Sedimentation of long-lasting wind-affected volcanic plumes: the example of the 2011 rhyolitic Cordón Caulle eruption, Chile

[1]C. Bonadonna, [2]R. Cioni, [2]M. Pistolesi, [3]M. Elissondo, [3]V. Baumann

[1], Section des sciences de la Terre et de l'environnement, Universitè de Genève, Suisse

Costanza.Bonadonna@unige.ch; Phone: +41 22 379 3055; FAX: +41 22 379 3601

[2], Dipartimento di Scienze della Terra, Università di Firenze, Italia

[3], Servicio Geológico Minero Argentino, Argentina

Abstract

Sedimentation processes and fragmentation mechanisms during explosive volcanic eruptions can be constrained based on detailed analysis of grain-size variations of tephra deposits with distance from vent and Total Grain-Size Distribution (TGSD). Grain-size studies strongly rely on deposit exposure and, in case of long-lasting eruptions, can be complicated by the intricate interplay between eruptive style, atmospheric conditions, particle accumulation and deposit erosion. The 2011 Cordón Caulle eruption, Chile, represents an ideal laboratory for the study of long-lasting eruptions thanks to the good deposit accessibility in medial to distal area. All layers analysed are mostly characterized by bimodal grain-size distributions, with both the modes and the fraction of the coarse sub-population decreasing rapidly with distance from vent and those of the fine sub-population being mostly stable. Due to gradually-changing wind direction, the two sub-

23 populations characterizing the deposit of the first two days of the eruption are

24 asymmetrically distributed with respect to the dispersal axis. The TGSD of the climactic

25 phase is also bimodal, with the coarse sub-population representing 90 wt.% of the whole

26 distribution. Polymodality of individual samples is related to size-selective sedimentation

27 processes, while polymodality of the TGSD is mostly related to the complex internal

28 texture (e.g. size and shape of vesicles) of the most abundant juvenile clasts. The most

29 representative TGSD could be derived based on a combination of the Voronoi tessellation

30 with a detailed analysis of the thinning trend of individual size categories. Finally,

31 preferential breakage of coarse pumices on ground impact was inferred from the study of

32 particle terminal velocity.

33

34

37

38

1. Introduction

Critical insights into eruption dynamics can be inferred from the study of the size of pyroclastic fragments, i.e. tephra (Kaminski and Jaupart 1998; Kueppers et al. 2006; Perugini et al. 2011; Rust and Cashman 2011; Dingwell et al. 2012). In addition, grain-size distributions and their variation with distance from vent can highlight important sedimentation processes that occurred during the eruption, e.g. particle aggregation and convective instabilities (Durant and Rose 2009; Durant et al. 2009; Brown et al. 2012; Carazzo and Jellinek 2012; Carazzo and Jellinek 2013). Finally, Total Grain-size Distribution (TGSD) represents a critical source parameter in numerical models for the description of tephra transport and sedimentation, used to compile both long-term hazard assessments and real-time forecasts crucial to mitigation strategies of volcanic risk. An accurate description of the amount of fine particles has also significant implications for the assessment of specific tephra hazards (e.g. impact on human and animal health, long-range threat to aviation, long-term ash resuspension) (e.g. Rose and Durant 2009). Nonetheless, the determination of TGSD is not straightforward due to: i) poor exposure of many tephra deposits, with very proximal and very distal areas being often of difficult access; ii) variable rate of deposit erosion; and iii) the complexity of integrating individual grain-size samples to derive the TGSD of the whole deposit (Bonadonna and Houghton 2005). TGSD of long-lasting eruptions is even more complicated by the combination of multiple pulses that are often not easy to correlate in the field and which are possibly associated with different mechanisms of magma fragmentation and clast dispersal.

Only a few TGSDs are available in the literature, and those available often lack either the fine or the coarse fraction, or both, and often represent a combination of multiple pulses (e.g. Rotongaio Ash (Walker 1981); Askja 1875 (Sparks et al. 1981); Mt St Helens

63   1980 (Carey and Sigurdsson 1982; Durant et al. 2009); Fuego 1974 (Murrow et al. 1980;

64   Rose et al. 2007); Etna 2001 (Scollo et al. 2007); Spurr 1992 (Durant and Rose 2009);

65   Eyjafjallajökull 2010 (Bonadonna et al. 2011); Pululagua 2450BP (Volentik et al. 2010); 4-

66   ka Rungwe Pumice (Fontijn et al. 2011)). Here we investigate the grain-size and

67   sedimentological features of the 2011 Cordón Caulle long-lasting eruption and assess the

68   uncertainties associated with the determination of the TGSD. A detailed characterization

69   of the stratigraphy and deposit features is presented by Pistolesi et al. (submitted).

70

71   **2. Stratigraphy and eruption evolution**

72   After about 41 years of repose, the Puyehue-Cordón Caulle volcanic complex (Central

73   Andes) erupted on June 4, 2011, from a system of vents located about 1500 m above sea

74   level (a.s.l.) on a NW-SE fracture of the Cordón Caulle system (Castro et al. 2013; Pistolesi

75   et al. submitted). This resulted in the evacuation of ca. 4,000 people in Chile and, due to

76   the prevailing winds, widespread disruption to various economic sectors and human

77   activities in Argentina (Collini et al. 2013; Wilson et al. 2013). The eruption developed as a

78   long-lasting rhyolitic activity with plume heights above the vent between ca. 9-12 km

79   above the vent during the first 3-4 days, 4-9 km during the following week and <6 km

80   after 14 June (GVP, Global Volcanism Program, http://www.volcano.si.edu; Siebert et al.

81   2010). The whole Cordón Caulle eruption was strongly affected by wind, with only the

82   first plume on June 4 being classified as subplinian (Mass Flow Rate of the order of ~10^7

83   kg/s), with the rest of the eruption being small-moderate with the cumulative volume of

84   the first 3-4 days characterized by a Volcanic Explosivity Index (VEI) of 5 (Bonadonna et al.

85   2015, in press). Thirteen tephra layers were identified, correlated and organized into four

86   Units based on lithologic characteristics, grain-size features and discontinuity surfaces;

4

87   satellite images were then used to correlate each Unit with specific eruptive phases

88   (Pistolesi et al. submitted).

89   Unit I (layers A to F) is a white to yellow lapilli-bearing deposit that represents the

90   coarsest Unit of the whole eruption (with B, D and F being the coarsest layers). It was

91   deposited towards the east-southeast on June 4 to 5 with negligible up-wind

92   sedimentation. The six layers are characterized by a distinct, multiple reverse grading, and

93   separated by planar discontinuities only evident in proximal-to-medial areas (<50 km

94   from vent) mainly marked by sharp grain-size changes. Farther from vent (25-50 km),

95   separation between the six layers becomes difficult to observe, and the deposit grades

96   into a single thin (<10 cm), massive, fine lapilli to coarse ash bed. The second eruptive

97   phase (June 5-6; Unit II with layers G and H) was marked by multiple wind shifts

98   depositing the obsidian-rich layer G towards the north and the distinctive light orange-

99   brown, pumice-rich layer H towards the east. Layer H was used as a marker to separate

100   Units I and II from Unit III. The third phase started on the morning of June 7 depositing

101   grey ash- to light-gray fine lapilli-bearing layers K1 to K5 towards the east (Unit III). This

102   phase was also associated with the emission of large ballistic bombs in proximal area

103   (Castro et al. 2013; Pistolesi et al. submitted). The fourth phase (Unit IV) deposited a thin

104   layer of white fine ash around the eruptive vent up to the southern slopes of Puyehue

105   volcano (i.e. 15 km from Cordón Caulle). No accurate time constraint could be made for

106   the fourth phase based on the deposit. Tephra is characterized by the abundance of

107   highly-to-extremely vesicular white pumice clasts, with minor banded and dense juvenile

108   fragments, which largely increase after the first phase (Unit I); lithic clasts are present

109   within Unit I and virtually absent in the following units. After the first three phases,

110   emission of low-intensity eruptive plumes, mainly dispersing ash, characterized the

111   eruption. However, more intense pulses of ash emissions were observed in July, October,

112   November 2011 and January 2012, which still caused disruption to aviation (Collini et al.

113   2013).

114

3. Methodology

116   The tephra deposit associated with the 2011 Cordón Caulle eruption was studied based

117   on ca. 70 outcrops located between 1 and 240 km from the active vent (see Pistolesi et al.

118   (submitted) for more details). Isopach maps for layers A-B, A-F, H and K2 were converted

119   into isomass maps based on mean values of deposit density, i.e. 560 kg m^{-3} for A-B and A-

120   F and 600 kg m^{-3} for H and K2 (Fig. 1) (see Pistolesi et al. (submitted) for details on isopach

121   maps). Selected samples of layers A-B, A-F, H and K2 were dried and weighed in the lab

122   and their volume was measured with a graduated cylinder in order to calculate the

123   deposit density. Samples collected for grain-size analysis were dried and mechanically

124   dry-sieved at half-ϕ intervals down to 0.5 mm (ϕ=-log$_2$D, where D is the particle diameter

125   in millimeters); the fine fraction (<0.5 mm) was characterized using a CILAS 1180 laser

126   particle size analyzer. The combination of sieving and laser-diffraction data was validated

127   on selected samples by overlapping data resulting from the two techniques for the

128   fractions between 0.5-0.063 mm. Mdϕ and sigma values were calculated according to

129   Inman (1952). 110 grain-size analyses of selected layers of Unit I, II and III were carried

130   out. However, given that the single layers forming Unit I (A-F) were only distinguishable

131   within 50 km from the vent, grain-size analyses of proximal outcrops were obtained based

132   on the thickness and density of each layer in order to obtain a cumulative A-F grain-size

133   distribution and investigate variations with distance from vent. Maps of lapilli fraction,

134   coarse-ash fraction and fine-ash fraction and of individual ϕ categories of the cumulative

6

135   Unit I (layers A-F) were then compiled (Fig. 2 and Appendix 1). Grain-size analyses were

136   also treated with the SFT (Sequential Fragmentation Transport; (Wohletz et al. 1989))

137   software to investigate single sub-populations. For almost all the analyzed samples, two

138   main sub-populations were identified, here indicated as sub-population 1 (SP1; coarse

139   grained) and sub-population 2 (SP2; fine grained), respectively. Componentry data,

140   juvenile density, morphological and textural analysis, vesicularity and chemistry are

141   reported and discussed in detail by Pistolesi et al. (submitted).

142

143   **4. Variations of grain-size with distance from vent**

144   In agreement with the isomass maps of the whole deposit (Fig. 1), a strong elongation

145   along the main wind direction is also shown by the isomass maps of individual size

146   classes, accompanied by a substantial lack of up-wind sedimentation (Fig. 2 and Appendix

147   1). Values of mass/area of Unit I are plotted on a log-axis versus distance from vent,

148   instead of square root of contour area, in order to investigate better sedimentation

149   trends and allow comparison with another deposit produced by a bent-over plume, i.e.

150   the 1996 Ruapehu eruption, New Zealand (Bonadonna et al. 2005) (Fig. 3); the detailed

151   comparison is presented in the discussion section. Lapilli clasts (diameter between 2-64

152   mm) are dispersed within the first 90 km from the vent with a load of more than 100 kg

153   m^{-2} within the first 40 km (Figs. 2a and 3a). Maximum accumulation of coarse ash is less

154   significant than for the lapilli clasts, being just over 30 kg m^{-2} within the first 45 km and

155   decreasing to 5 kg m^{-2} around 110 km from vent (Figs 2b and 3a). Fine ash represents the

156   predominant size fraction beyond 100 km from vent (see for example the maps of lapilli

157   and coarse ash; Figs. 2 and 3a). Isomass maps of individual ϕ categories confirm that the

158   low abundance of coarse ash is mainly related to the scarce sedimentation of particles in

159   the 3ϕ class (250-125 μm), while ash in the categories 4ϕ and ≥5ϕ categories (between

160   63-125 μm and <63 μm) clearly extend beyond 250 km from vent (Appendix 1). Multiple

161   accumulation maxima are clearly visible only in the fine-ash map, with the two most

162   significant being located around 20 and 100 km from vent. However, these multiple

163   maxima are not visible in the total deposit map (Figs 2c and 3a).

164   Detailed analyses of individual samples highlight a rapid decay of mean grain-size for

165   all layers from proximal (Mdϕ=-3.5, -1.6 and -0.8 for A-F, K2 and H respectively) to distal

166   samples (Mdϕ=5 for A-F and K2), followed by a less steep decrease between 50 and 250

167   km (Fig. 4a). Between 50 and 120 km from vent, Mdϕ values range between 0.5-5.2 for A-

168   F and K2 and between 4.8-5.2 for H, reaching 5.4 at our most distal sample of A-F and K2

169   (i.e., 240 km from the vent) (Fig. 4a). Sorting does not show any clear trend with distance

170   from vent, varying between 0.3-2.9 for A-F (very well sorted to poorly sorted), 0.7-2.4 for

171   H (very well sorted to poorly sorted) and 1.2- 3.3 for K2 (well sorted to poorly sorted) (Fig.

172   4b). Many of these values stay at the upper limit of the fallout field of the Mdϕ-$\sigma\phi$ of

173   Fisher and Schmincke (1984). A detailed analysis of the sorting data shows how the best

174   sorted samples (mostly for A-F and H) are those associated with the deposit south of the

175   dispersal axis (Fig. 4b). Due to a clear increase of particle density with the decrease of

176   particle size (Pistolesi et al. submitted), the increase of the Mdϕ value with distance from

177   vent is the main cause for the increase of deposit density (Fig. 5). In fact, deposit density

178   varies between 330 and 920 kg m^{-3} between about 24 and 240 km from vent. However,

179   the most rapid change (from 330 to 790 kg m^{-3}) is observed between 24 and 50 km from

180   vent, where Mdϕ has the largest variability (Figs. 4a and 5). The correlation of deposit

181   density with Mdϕ is remarkably linear (i.e. exponential with the representative particle

182   diameter in mm) (Fig. 5b).

183   Most of the sampled deposits (A-F, H and K2), with the exception of our most distal

184   sample at 240 km from vent, are characterized by a clear grain-size bimodality, which can

185   be deconvoluted into two main Gaussian sub-populations (SP1 and SP2) using the SFT

186   software (Fig. 6). The weight fraction associated with the coarse sub-population (SP1) is

187   >75% for most samples south of the dispersal axis (Fig. 6a), which are also characterized

188   by the best sorting (Fig. 4b). The mode of SP1 decreases with distance from the vent from

189   -2.6 to 1.8ϕ (between 15-100 km from vent) and within the first 100 km it mostly

190   coincides with Mdϕ values of the whole samples (Figs. 4a and 6b). The decay trend of SP1

191   is similar for all layers, with A-F being typically the coarsest and H the finest through the

192   whole deposit (Fig. 6b). The mass loading of SP1 of all layers decreases regularly with

193   distance from vent, going from about 455, 38 and 84 kg m^{-2} at 15-20 km from vent (for A-

194   F, H and , K2 respectively) to <10 kg m^{-2} beyond about 80 km from vent for all layers and

195   even to <0.1 kg m^{-2} for layer H (Fig. 7a). In contrast, the mode of the fine-grained sub-

196   population (SP2) remains nearly constant between 4.5-5.9ϕ (Fig. 6b), while the decay of

197   the mass loading is less regular than for SP1, and always remains between 0.1-15 kg m^{-2}

198   (Fig. 7b). The samples with the highest mass loading for SP1 are those south of the

199   dispersal axis (Fig. 7a). Layer H is characterized by the smallest SP2, which varies between

200   0.3-1.4 kg m^{-2} throughout the whole deposit (i.e., 15-104 km from vent; Fig. 7b).

201   Nonetheless, beyond 50 km from the vent, SP2 of H samples is always more abundant

202   (0.3-0.6 kg m^{-2}) than the associated SP1 (<0.1 kg m^{-2}).

203   Grain-size variations are asymmetrically distributed across the dispersal axis, the

204   relative abundance of SP1 in the southern samples being larger than that of the northern

205   samples (Fig. 8). This is particularly evident in samples from Unit I (A-F layers) and can

206　explain the poor correlation of $\sigma\phi$ with distance from vent (Fig. 4b), the relative amount

207　of SP1 and SP2 (Fig. 6a) and the corresponding mass loadings (Figs. 7).

208

5. Distribution of terminal velocity

209

210　In order to investigate particle sedimentation, terminal velocity was determined for the

211　coarse clasts (-4.5 to 0 ϕ) that fell at a locality 15 km downwind from the vent along the

212　dispersal axis (Fig. 9 and Appendix 2). First, the clasts were grouped into two different

213　density categories based on the detailed componentry and density analysis carried out by

214　Pistolesi et al. (submitted): a high-constant density category, and a variable size-

215　dependent density category (for 4.5 to 0ϕ: 435 to 978 kg m^{-3}, layers A to F, Fig. 9b; 440 to

216　863 kg m^{-3}, layer H, Fig. 9e; 460 to 1016 kg m^{-3}, layer K2, Fig. 9h). The high-density

217　category combines clasts with high-constant density (2,700 kg m^{-3}), i.e. lithic and obsidian

218　fragments, while the variable size-dependent density category consists of juvenile

219　fragments with variable vesicularity, i.e. banded pumice clasts, dense juvenile clasts and

220　white pumice clasts (componentry classes defined as in Pistolesi et al. (submitted)).

221　Clasts in the range -4.5-0ϕ represent about 90 wt.% of the deposit of all samples

222　considered at this location, practically coinciding with SP1 (Fig. 9). Componentry plots also

223　show that high-density clasts are most abundant within the finest size categories (i.e. 0 to

224　-3.5ϕ for A-F and 0 to -1.5ϕ for H and K2), with the coarsest categories being mostly free

225　of high-density clasts (i.e. -4.0 to -4.5ϕ for A-F and -2 to -4ϕ for H and K2) (Figs. 9a,d,g and

226　Appendix 2). Polymodality of the grain-size distribution largely disappears when clast size

227　is converted into terminal velocity, which peaks at a single value for all layers. The peak

228　value mostly depends on plume height, i.e. ~20 m/s for A-F, ~15 m/s for H and ~10-15

229 m/s K2 (maximum plume height of 14 km, 12 km and 10 km for A to F, H and K2

230 respectively).

231   It is also interesting to note how the spread of all velocity distributions is significantly

232 narrower than that of grain-size. When both high-density clasts and variable-density

233 clasts are normalized to 100 and plot together, it is clear how, individually, they cannot

234 always be described by a Gaussian distribution (Figs. 9c,f,i and Appendix 2). In addition,

235 the two density categories overlap in the central velocity classes, whereas the highest and

236 the lowest velocity classes are only represented by high-density and variable-density

237 clasts, respectively, with mostly no overlap on the tails (bins of Fig. 9). In particular, the

238 distribution of the variable-density clasts (i.e. juvenile vesicular clasts) seems to be shifted

239 by about one bin category towards the low-velocity values (based on 5 m/s binning; Figs.

240 9c,f,i and Appendix 2). This suggests an excess of clasts smaller than the modal size,

241 probably related to clast breaking upon impact with ground. High-density clasts, less

242 prone to break, do not show this feature, and their terminal velocity frequency

243 distribution is generally much less peaked (more platykurtic) than that of variable-density

244 clasts (Appendix 2). Based on the shift of the peak value of A-F from 20 m/s (high-density

245 clasts) to 15 m/s (variable-density clasts) (i.e. reduction of mean diameter value from ~28

246 to ~13 mm; Fig. 9), we can derive that the diameter of variable-density clasts was reduced

247 by about 50% due to clast breakage. Breakage seems to be much more effective for large

248 clasts, as evidenced by the general lack of variable-density clasts with high terminal

249 velocity.

250

251 **6. Total grain-size distribution**

252   The TGSD was determined for the climactic phase of the Cordón Caulle eruption based on

253   different strategies: i) Voronoi tessellation (Bonadonna and Houghton 2005); ii) weighted

254   average; and iii) mass of individual ϕ categories (Fig. 10 and Table1). The mass of

255   individual ϕ categories was derived in three different ways: a) integration of the

256   exponential and b) Weibull fitting of the isomass maps of individual ϕ categories of

257   Appendix 1 (Pyle 1989; Bonadonna and Costa 2012); and c) inversion of values of

258   mass/area of individual ϕ categories using the model TEPHRA2 following Volentik et al.

259   (2010). Particles <4ϕ were not considered in the last technique, as size-selective

260   processes, such as particle aggregation and convective instabilities, cannot be currently

261   described by inversion strategies (Fig. 10b and Appendix 4). The Voronoi tessellation was

262   applied to two data sets: the complete data set of all our A-F samples (dataset 1) and the

263   combination between dataset 1 and six additional distal points (around 610 km from

264   vent) derived from two isopach maps compiled soon after the eruption that account for

265   the distal deposit (dataset 2) (see Appendix 3 for details). We have assigned to these six

266   distal points a grain-size distribution based on the relative proportion of lapilli, coarse ash

267   and fine ash as derived from Fig. 3a. In fact, the best fit of the three size fractions

268   considered, indicates that around 610 km from vent the deposit mostly consists of fine

269   ash (see Appendix 3). Nonetheless, even if six distal samples are reconstructed and

270   considered in the calculation, the resulting grain-size does not change significantly (Fig.

271   10a and Table 1). Relative increase in fine ash for dataset 2 with respect to dataset 1 is ~4

272   wt.% (i.e., 13 wt.% and 9 wt.%, respectively; Table 1). Not enough grain-size data were

273   available to determine the TGSD of layers H and K2.

274   All strategies result in polymodal distributions with a clear lack of particles in the 3ϕ

275   category, which is always <1 wt.%. However, while the TGSD resulting from the Voronoi

276 tessellation, weighted average and inversion strategies are mostly bimodal with similar

277 Mdϕ and sorting values (Table 1), the TGSD derived from the mass associated with

278 individual ϕ categories are more complex and polymodal, regardless of whether the

279 associated mass is determined based on the exponential or the Weibull fitting. The TGSD

280 derived with the Voronoi tessellation strategy is slightly coarser than the weighted

281 average strategy because the Voronoi tessellation allows for a better representation of

282 individual outcrops even when the distribution is not uniform, as is the case for the

283 proximal samples from the Cordón Caulle eruption (e.g. Fig. 1). The TGSD derived with the

284 inversion is also coarser, mostly because the fine-ash fraction could not be considered in

285 the calculation (i.e. particle <4ϕ). In all cases, TGSD shows two main sub-populations. The

286 modal value of the coarse sub-population is consistent for all datasets and strategies,

287 with the exception of the exponential and Weibull integrations (i.e. -1.9 to -2.5ϕ; Table 1).

288 The advantage of the inversion on grain-size with respect to the inversion on

289 mass/area and the other strategies to derive TGSD is the derivation of the plume height,

290 which, in the case of the climactic phase of the Córdon Caulle eruption resulted in an

291 average best-fit value of ~14 km a.s.l. with most particles being released between ~9-10

292 km a.s.l., in agreement with observations (Appendix 4) (targeted inversion on mass/area

293 resulted in average plume height of ~13 km a.s.l.; Bonadonna et al. 2015, in press).

294 However, the Root Square Mean Error (RSME) minima associated with the best-fit values

295 of plume height for the climactic phase of the Córdon Caulle eruption are not as well

296 constrained as when applied to plumes developing in almost no wind (e.g. Pululagua 2450

297 BP Plinian eruption, Ecuador (Volentik et al. 2010), ~4-ka Rungwe Pumice Plinian

298 eruption, Tanzania (Fontijn et al. 2011)). In fact, similarly to mass/area inversion

299 (Bonadonna et al. 2015, in press), the erupted mass of individual size categories is better

300 constrained than plume height (Appendix 4). This is probably due to the stronger

301 influence of wind entrainment on the plume rise, which increases the complex interaction

302 amongst input parameters.

303

304 **7. Discussion**

305 The 2011 Córdon Caulle eruption represents an ideal case study to investigate grain size

306 and sedimentological features of long-lasting eruptions and to assess the complexities

307 and uncertainties associated with the determination of the associated TGSD.

308

309 *Particle sedimentation*

310 As shown by our study, grain-size features vary significantly based on distance from the

311 vent, eruptive style, intensity and atmospheric conditions (e.g. Figs. 3 to 8). Further

312 complexities in sedimentation can be added by the presence of multiple sub-populations

313 in the TGSD, as is the case for the climactic phase of the Cordón Caulle eruption. This has

314 obvious implications on the long-term assessment of eruption impact, including impact

315 on human and animal health, impact on vegetation, generation of secondary lahars and

316 ash resuspension. Grain-size variation and mass accumulation with distance from vent

317 can also be significantly affected by specific sedimentation processes, such as particle

318 aggregation and convective instabilities. In order to investigate the general trend of

319 particle deposition, we compare the sedimentation of the Cordón Caulle Unit I (plume

320 height of 11-14 km a.s.l. and average wind speed along plume rise of ~20 m s^{-1};

321 Bonadonna et al. 2015, in press) with the sedimentation from another eruption strongly

322 affected by wind for which detailed grain-size data are also available: the Ruapehu 1996

323 eruption, New Zealand (Fig. 3b).

324 The Ruapehu eruption was characterized by a smaller erupted mass, a slightly lower

325 plume and a slightly higher wind speed than the climactic phase of the Cordón Caulle

326 eruption (plume height of 8.5 km a.s.l. and average wind speed along plume rise of ~24 m

327 s^{-1}; (Prata and Grant 2001; Bonadonna et al. 2005)). However, the three main size

328 fractions show a very similar thinning trend (i.e. lapilli, coarse ash and fine ash) (Fig. 3). In

329 fact, even though the total A-F deposit can be fitted by at least two exponential segments

330 on a semi-log plot of mass/area versus distance from vent, individual size fractions could

331 be well fitted by single exponential segments with slopes that are similar to those of the

332 Ruapehu deposits (slope values for Cordón Caulle/Ruapehu: -0.108/-0.108 for lapilli

333 clasts, -0.027/-0.023 for coarse ash, -0.004/-0.005 for fine ash; Fig. 3). Due to the

334 presence of an active lava flow emplaced during the eruption that could not be crossed

335 during the field surveys, we could not collect data in the proximal downwind sector of

336 Cordón Caulle (<15 km from the vent), precluding the possibility to recognize the most

337 proximal exponential segments that can be identified at Ruapehu (Fig. 3b). The most

338 distal break-in-slope for both cumulative thinning trends is associated with the

339 intersection between the coarse-ash and the fine-ash trends (i.e., 110 km and 150 km

340 from vent for Cordón Caulle Unit I and Ruapehu, respectively; Fig. 3). Due to a smaller

341 erupted mass (5×10^9 kg), smaller accumulations are observed for Ruapehu at any distance

342 from vent (Fig. 3b). In addition, probably due to the lower plume, sedimentation of lapilli

343 clasts is mostly confined within the first 10 km for the Ruapehu deposit, which results in a

344 different relative proportion of the size components at any distance from vent. As an

345 example, the relative proportions of lapilli clasts, coarse ash and fine ash at about 40 km

346 from vent is 56%, 33% and 11% for Cordón Caulle A-F and 1%, 83% and 16% for Ruapehu

347 (total accumulation being about 90 and 1 kg m^{-2} for the two deposits, respectively). Fine

348 ash becomes dominant for both deposits beyond 200 km from vent with a similar decay.

349 The similar deposit features shown by the Cordón Caulle Unit I and the Ruapehu

350 eruptions, suggest that sedimentation from bent-over plumes is associated with similar

351 thinning decay with distance from vent, even though the accumulation at any distance

352 from vent is directly proportional to the total erupted mass and the relative fractions of

353 lapilli clasts, coarse ash and fine ash, which might change depending on plume height

354 (with higher plumes dispersing coarse particles further from vent). It is also important to

355 bear in mind also that the Ruapehu eruption was mostly associated with a unimodal and

356 coarser TGSD, and, therefore, the thinning trend of size fractions seems to be

357 independent from source conditions. We stress how such a detailed analysis of the

358 thinning trend of individual size categories can provide insights into the grain-size

359 distribution of distal deposits (e.g. Fig. 3 and Appendix 3). As an example, such a critical

360 analysis clearly shows how the deposit mostly consists of fine ash beyond 200 km, where

361 the coarse ash is only about 0.5 kg m^{-2} (15% of the total loading).

362

363 *Grain-size bimodality*

364 The layers analyzed in detail, i.e. A-F (4-5 June), H (6 June) and K2 (7 June) were all mostly

365 characterized by bimodal grain-size distributions. Similarly, samples collected from the

366 entire A-F sequence all have the same grain-size features, evidencing no significant

367 changes through the sequence (Pistolesi et al. submitted). An interesting feature is the

368 decrease in grain-size of the SP1 mode with distance from vent for all layers and the

369 stable mode of SP2 around 4-6ϕ (Fig. 5b), which has already been observed in other

16

370   tephra deposits (e.g. Montserrat, West Indies; St Vincent, West Indies; El Chichon, Chile;

371   Mt St Helens, USA; Mt Mazama, USA (Brazier et al. 1983; Varekamp et al. 1984;

372   Bonadonna et al. 2002; Durant et al. 2009; Brown et al. 2012; Durant et al. 2012).

373   However, a more interesting aspect is the poorly variable mass loading (0.1-15 kg m^{-2}) of

374   SP2 that does not show any obvious trend with distance from vent and with the mass

375   loading of SP1 (Fig. 6b), although samples collected south of the dispersal axis generally

376   have a lower mass loading with respect to samples from similar distances collected north

377   of the axis. While the regular decrease of the SP1 mode with distance from vent suggests

378   normal settling of individual clasts dominated by plume height and wind advection, the

379   ubiquitous presence of a fine sub-population with a constant grain-size distribution is

380   interpreted as an evidence of settling dominated by size-selective sedimentation

381   processes (e.g. particle aggregation and/or convective instabilities) that may have

382   affected particle fallout even 15 km from the vent.

383   Particle aggregates were only observed within the K1 deposit at a few sites close

384   to Villa La Angostura (48 km from the vent) (i.e. millimetric structured accretionary

385   pellets; Pistolesi et al. submitted), suggesting that fine ash mostly fell as very fragile

386   aggregates whose structure was not preserved during impact with ground (Brown et al.

387   2012). Unfortunately, we could not sample the deposit in more proximal areas to verify if

388   aggregation occurred at distances <15 km and, if so, in which form. Premature fallout of

389   fine particles can also be associated with convective instabilities often observed during

390   sedimentation of small-moderate eruption plumes, which could also enhance particle

391   aggregation due to the increased particle concentrations within the resulting fingers

392   (Bonadonna et al. 2002; 2005; 2011; Carazzo and Jellinek 2013; Manzella et al. 2015, in

393   press). Convective instabilities are expected to have played an important role also during

394   the Cordón Caulle eruption, even though no clear pictures of downwind sedimentation

395   during the climactic phase of the first few days are available to confirm this hypothesis.

396   Considering that A-F, H and K2 layers were generated by plumes with different intensities,

397   we conclude that aggregation and/or convective instabilities were persistent processes

398   throughout the whole eruption, not significantly affected by small differences in plume

399   height.

400   A persistent sub-population of fine particles generating bimodal grain-size distribution

401   has also sometimes been reported as being generated by co-PDC plumes (Carey and

402   Sigurdsson 1982; Bonadonna et al. 2002; Eychenne et al. 2012). However, Cordón Caulle

403   PDCs had runout distances too short (i.e. ~10 km) and possibly volumes too small (ca.

404   10% of A-F total deposit; Pistolesi et al. submitted) to disperse a significant amount of fine

405   ash up to 100 km from vent where bimodality is still observed (Pistolesi et al. submitted).

406   In addition, PDCs were only observed on 4, 5 (with a runout of ~10 km;

407   (SERNAGEOMIN/OVDAS 2011)), 8 and 14 June, whereas layers H and K2 also show

408   bimodal distributions and they were produced on 6-7 June 2011. However, we do not

409   exclude that part of the ash component in the proximal A-F deposit (generated on 4-5

410   June) could be a combination of co-PDC and main plume fallout.

411   Finally, grain-size bimodality also affects deposit sorting. In fact, sorting is typically

412   improved by wind advection, with tephra deposits generated during low-wind conditions

413   being usually poorly sorted. However, this is not the case for the Cordón Caulle eruption.

414   As an example, the Pululagua 2450 BP Plinian eruption, Ecuador (Volentik et al. 2010) and

415   the ~4-ka Rungwe Pumice Plinian eruption, Tanzania (Fontijn et al. 2011) are

416   characterized by sorting between 1.1-3.0 and 1.3-2.0, respectively, which are in the same

417   range shown by layers A-F, H and K2 (i.e. 0.3-2.9, 0.6-2.4 and 1.2-3.3, respectively; Fig.

418   4b). For the two no-wind eruptions, sorting seems to improve with distance from vent

419   (particularly for the Pululagua eruption) and the associated TGSD is mostly unimodal.

420   Regardless of the strong wind advection, sorting at Cordón Caulle is not significantly

421   better than for the Pululagua and Rungwe Pumice eruptions, most probably because of

422   the bimodality of grain-size distributions at all outcrops (e.g. Fig. 6).

423   The sorting of the deposits of the climactic phase of the Cordón Caulle eruption was

424   shown to be worst north of the dispersal axis due to a strong asymmetry of the

425   distribution of the two sub-populations SP1 and SP2 (Fig. 8). Such an asymmetry was also

426   observed for the small-moderate Mt St Helens eruptions (USA) on May 25 through August

427   7, 1980, which was explained as mostly due to distribution-rotation of wind direction with

428   altitude, and variability in the duration, height, and qualitative density of eruption

429   columns (Waitt et al. 1981). Similarly, the preferential accumulation of SP1 and SP2 south

430   and north of the dispersal axis, respectively, can be related to the progressive wind shift

431   towards the north that occurred at the end of June 5 associated with a lowering of the

432   plume height (e.g. Bonadonna et al. 2015, in press; Pistolesi et al. submitted).

433

434   *Secondary maxima of accumulation*

435   Multiple maxima of accumulation are shown by the fine-ash fraction of the A-F deposit of

436   Cordón Caulle, but not by the total deposit (Figs. 2, 3 and Appendix 1). Secondary maxima

437   of accumulation of the total deposit have often been associated with particle aggregation

438   (e.g. Mt St Helens 1980 (Carey and Sigurdsson 1982; Durant et al. 2009); Hudson 1991

439   (Scasso et al. 1994); Quizapu 1932 (Hildreth and Drake 1992)). Multiple maxima of

440   accumulation were also observed in the fine-ash fraction of the deposit associated with

441   the Ruapehu 1996 plume, New Zealand, for which particle aggregation was not so evident

19

442 in the deposit but that was also strongly distorted by wind advection (Bonadonna et al.

443 2005). However, in the Ruapehu case, these multiple maxima coincide with multiple

444 maxima in the total deposit (Fig. 3b). Even though, both for the Cordón Caulle eruption

445 and the Ruapehu eruption, aggregation processes were not evident in the associated

446 deposit, secondary maxima of accumulation are clearly related to size-selective

447 sedimentation processes that affect only particles ≤63 μm. These processes are most

448 likely related to particle aggregation and convective instabilities even when field evidence

449 is missing. As an example, particle aggregation has been shown to generate fragile

450 clusters that easily break on impact with the ground (e.g. Brown et al. 2012). Finally,

451 considering that tephra deposits are not always investigated based on isomass maps of

452 individual grain-size categories, we can conclude that the fine-ash fraction tends to

453 produce secondary maxima of accumulation even when these are not shown by the total

454 tephra deposit.

455

456 *Total Grain-Size Distribution*

457 Our results show how the Voronoi tessellation, weighted average and inversion strategy

458 give more consistent results for TGSD than the strategies based on the mass calculated

459 from empirical fits (i.e. exponential and Weibull fits). This is due to the poor distribution

460 of mass/area points for individual ϕ categories that result in isomass maps with mostly ≤3

461 contours (Appendix 1). Four and five contours could be well identified only for -1 and 0ϕ.

462 The mass associated with 3ϕ had to be calculated with the method of Legros (2000) as

463 only one contour could be drawn. The cumulative mass derived with the exponential and

464 Weibull method is about 60% and 75%, respectively, of the total mass derived from the

465 isopach map of the cumulative deposit of Pistolesi et al. (submitted) (i.e., ~2.8 and

466   3.7x10^{11} kg versus ~5x10^{11} kg). In addition, the Voronoi tessellation for the derivation of

467   TGSD is preferred with respect to the weighted average because it can better characterize

468   non-uniform point distributions (as shown by the higher sensitivity to the addition of 6

469   distal points; Fig. 10 and Table 1) and to the inversion of individual size categories

470   because this cannot be applied to the fine-ash fraction that is likely to be affected by size-

471   selective sedimentation processes (e.g. particle aggregation). In addition, the application

472   of inversion strategies to eruptions strongly affected by wind entrainment seems to be

473   more complex than the application to strong plumes (see also Bonadonna et al. 2015, in

474   press). The TGSD of the A-F deposit as derived with the Voronoi tessellation applied to

475   the dataset 1 is clearly bimodal, with the two main sub-populations peaked at -2.5 and

476   6.2ϕ, a large fraction of the coarse population (90 wt.%) and a significant low cumulative

477   wt.% (0.8) of particles between 0.250-0.125 mm (i.e. 2-3ϕ) (Table 1).

478   Polymodality of TGSD has already been observed for other tephra deposits (e.g.

479   Montserrat Vulcanian and dome collapse explosions (Bonadonna et al. 2002); Mt St

480   Helens 1980 (Carey and Sigurdsson 1982; Durant et al. 2009); Mt Spurr 1992 (Durant and

481   Rose 2009); Tunguragua 2006 (Eychenne et al. 2012); El Chichon 1982 (Varekamp et al.

482   1984); Pinatubo 1991 (Wiesner et al. 2004); 1979 Soufriere St Vincent, Mazama 7000 a.

483   (Brazier et al. 1983)), for which it could be explained as mainly due to the contribution of

484   sedimentation from co-PDC plumes. However, as already mentioned above, we consider

485   the contribution of co-PDC sedimentation to be very limited for the Cordón Caulle

486   eruption. In addition, such a striking polymodality is in contrast, for example, with the

487   TGSD of another rhyolitic Plinian eruption (β layer, Chaitén 2008 eruption, Chile; (Alfano

488   et al. submitted)), which is characterized by one single population peaked around 6ϕ, i.e.

489   mostly coinciding with the fine population of the A-F deposit. Considering that both

21

490   eruptions have been studied in detail and the TGSD has been integrated over a similar

491   deposit extension (up to about 600-800 km from source) and with the same

492   methodologies, we believe that the striking differences are related to the actual

493   fragmentation of the erupted material. In particular, it is important to bear in mind that

494   about 80 wt.% of the β layer of the 2008 Chaitén eruption consists of non-vesicular

495   material and that the associated vesicular juveniles are characterized by a unimodal

496   vesicle size distribution (Alfano et al. 2012). Fragmentation of such homogeneous

497   pyroclastic material is more likely to result in one single population than the

498   fragmentation of polycomponent material characterized by juveniles with complex vesicle

499   textures, such as that of Cordón Caulle Unit I (Pistolesi et al., submitted; Schipper et al.,

500   2013). Given the abundance of white-pumice clasts in the A-F cumulative layer of Cordón

501   Caulle, we conclude that the grain-size polymodality is mostly due to the associated

502   complex texture. In fact, white-pumice clasts are characterized by the coexistence of

503   spherical and nearly isotropic vesicles together with vesicles with highly deformed and

504   convoluted shapes (Pistolesi et al. submitted), which, when fragmented, are likely to

505   result in multiple distinct peaks of particle sizes.

506

507   *Terminal velocity*

508   Our detailed analysis of terminal velocity at the reference outcrop 15 km from vent has

509   shown how particles deposited at a given location are peaked around a characteristic

510   velocity that mostly depends on plume height and particle density (Fig. 9 and Appendix 2;

511   to note that maximum plume heights were considered for all calculations and therefore

512   particle terminal velocities are to be considered as maximum values). However, high-

513   density and variable-density particles show different modal values for terminal velocity,

generally overlapping only in a few central velocity classes. We have interpreted such a

shift of the moderately to highly vesicular, variable-density clasts towards the low velocity

categories as due to an important effect of clast breakage on impact with the ground.

Based on the shift of the peak velocity values, we estimated such a breakage to be about

50% of the original diameter of the variable-density clasts.

This has important implications both for the determination of the largest clasts

and of the TGSD. In fact, our results clearly support the recommendation of the collection

of largest lithics as supposed to largest pumices for the compilation of isopleth maps

(Sparks et al. 1981; Bonadonna et al. 2013). In addition, given the absence of variable-

density clast sizes corresponding to the largest velocities, and to the evident increment of

clasts in the modal terminal velocity (evidenced by the frequency distribution of terminal

velocities for these clasts, highly peaked on a modal class with terminal velocity values

equal or slightly lower than those of lithic fragments), we suggest that the coarsest

variable-density clasts are the most affected by breakage at impact.

Considering that tephra deposits of subplinian-Plinian eruptions are typically mostly

composed of variable-density (juvenile) clasts (e.g. variable-density clasts of A-F are ~73%

of the total deposit; Fig. 9 and Appendix 2), we can also conclude that TGSD derived from

tephra deposits are very likely to be shifted towards lower size values, with a possible

general underestimation of the coarse clasts contribution. Dufek et al. (2012) have

already shown the relation between amount of fine ash and fragmentation depth due to

collisional processes in the conduit. Here we show how additional breakage of lapilli clasts

can occur on ground impact, inducing a shift in the calculated TGSD. This has important

implication for the associated discussion of magma fragmentation and simulations of

particle dispersal.

538

Deposit erosion and particle resuspension

540   Long-lasting eruptions are characterized by a complex interplay between tephra

541   accumulation and deposit erosion depending also on local soil and atmospheric

542   conditions (e.g. rain, snow, wind, vegetation cover, soil moisture). As an example, due to

543   persistent strong winds, significant resuspension of the distal part the Córdon Caulle

544   deposit affected air quality and resulted in the closure of important airports even months

545   after the beginning of the eruption (e.g. 14-18 October 2011 (Wilson et al. 2013; Folch et

546   al. 2014)). These resuspension events have also been recognized in other ash-rich

547   deposits (e.g. Katmai, USA (Hadley et al. 2004); Mount St Helens, USA (Hobbs et al. 1983);

548   Hudson, Chile (Wilson et al. 2011); Montserrat, West Indies (Hincks et al. 2006);

549   Eyjafjallajökull, Iceland (Leadbetter et al. 2012; Thorsteinsson et al. 2012)) and can be

550   comparable to the dispersal of primary ash fallout in terms of dispersal area, with the

551   potential to cause widespread impact on agriculture, aviation, livestock and human health

552   long after a volcanic eruption and far away from the original eruptive vent.

553   The source term necessary to model and forecast resuspension events can only be

554   characterized by a detailed study of the tephra deposit that can be potentially

555   remobilized by strong winds. Local grain-size distribution is likely to be very different from

556   the TGSD of the eruption and can only be constructed based on a selection of critical

557   outcrops. As a result, detailed stratigraphic studies of tephra deposits and the physical

558   characterization of eruptive parameters becomes the first step to develop effective

559   mitigation strategies and land-use planning. Resuspension mostly affected layers K1-K5

560   (Unit III) of the 2011 Córdon Caulle deposit, which are the only layers that were found

561   remobilized during our last field survey (i.e. February 2013). In fact, comparison between

24

562 observations made during the first surveys (i.e. July 2011 and October-November 2011)

563 with observations made in May 2012 and February 2013 show that erosion did not affect

564 layers A to H. In addition, Layers K1-K5 are mostly characterized by particles with

565 diameter <250 μm, which was considered by Folch et al. (2014) as a threshold for

566 resuspension for the Córdon Caulle deposit. The total thickness of remobilized material

567 was then <0.5 cm. In general, a thinning plot showing the trend of the fine-ash fraction

568 (e.g. Fig. 3a) can be used to derive the approximate amount of material that can be

569 remobilized at any given distance.

570

571 **8. Conclusions**

572 In this paper we focus on particle size and sedimentation processes during the first

573 eruptive phases of the 2011 Cordón Caulle eruption (i.e., June 4-7, 2011). Based on our

574 detailed field campaigns and analytical studies we can conclude that:

575 1) All layers analysed (i.e., cumulative layer A-F, H and K2) are mostly characterized by

576 bimodal grain-size distributions, with the mode of the coarse sub-population (SP1)

577 decreasing rapidly with distance from vent (from -2.6 to 1.8ϕ between 15-100 km from

578 vent) and the associated mass fraction varying from about 500 kg m^{-2} (15 km from

579 vent) to <10 kg m^{-2} (beyond 100 km from vent). In contrast, the mode of the fine sub-

580 population (SP2) remains stable between 4.5-5.9ϕ with a mass loading always between

581 0.1-15 kg m^{-2}.

582 2) The fine sub-population has been interpreted as being mostly associated with size-

583 selective sedimentation processes (e.g. particle aggregation, convective instabilities)

584 confirmed by the presence of multiple accumulation maxima associated with the fine-

585 ash fraction (i.e. particles <63 μm). Considering the similarity of grain-size features and

586   trends for the three layers analysed, patterns of fine-ash sedimentation during the

587   Cordón Caulle eruption can be interpreted as being independent of plume height and

588   eruptive style.

589 3) The presence of multiple maxima of accumulation for the fine-ash fraction but not

590   shown by the total deposit suggests that size-selective sedimentary processes play an

591   important role in most eruptions even when multiple maxima are not shown by the

592   total deposit.

593 4) The coarse and fine sub-populations of the A-F layers are asymmetrically distributed

594   with respect to the dispersal axis, with SP1 being more abundant in the southern

595   samples. This is probably related to the progressive shift of the wind direction towards

596   the north, which occurred at the end of the deposition of Unit I associated with a

597   lowering of plume height (June 5).

598 5) The rapid decrease of Mdϕ within the first 50 km is associated with a rapid increase of

599   deposit density from from 330 to 790 kg m^{-3}. The highest value of deposit density

600   observed is 920 kg m^{-3} at 240 km from vent (A-F layers).

601 6) The combination of Voronoi tessellation with a detailed analysis of the thinning trend

602   of individual size categories (e.g. lapilli clasts, coarse ash and fine ash) was considered

603   to provide the most representative TGSD of the climactic phase of the Cordón Caulle

604   eruption, which is characterized by two main sub-populations peaked at -2.5 and 6.2ϕ,

605   with the coarse sub-population representing about 90 wt.% of the whole distribution.

606 7) Detailed investigations have shown that the grain-size bimodality is not related to the

607   lack of distal samples but to a significant lack of particles in the 3ϕ category. The

608   addition of distal samples (600 km from vent) only slightly increases (<5 wt.%) the

609   amount of fine ash. We suggest that the shape of the TGSD record a primary

610   fragmentation process possibly related to the complex textural features of the highly

611   vesicular magma.

612   8) The derivation of TGSD based on weighted average and on the mass of individual size

613   categories as derived from empirical fits and analytical inversions were of more

614   difficult application and did not provide exhaustive results. The analytical inversion

615   could provide important insights into plume height, but should be used with caution

616   when applied to eruptions strongly affected by wind entrainment.

617   9) Bent-over plumes of both Cordón Caulle (June 4-5) 2011 and Ruapehu 1996 eruptions

618   are characterized by similar sedimentation patterns, with thinning of lapilli, coarse ash

619   and fine ash being described by exponential segments with similar slope. However, the

620   relative fraction of individual components and the position of the break-in-slope might

621   vary mostly depending on erupted mass and plume height.

622   10)   Particle sedimentation at different distances from the vent can be described by a

623   Gaussian distribution of terminal velocity with a mode that mostly depends on plume

624   height and particle density. Nonetheless, we have observed a shift between high-

625   density clasts and variable size-dependent density clasts at a same outcrop, mainly due

626   to preferential breakage of coarse vesicular pumices at impact with the ground. We

627   conclude that TGSDs derived from tephra deposits rich in highly vesicular juvenile

628   material can be biased towards fine fractions generated during deposition in relation

629   to the physical and textural features of the clasts (vesicularity, thermal history,

630   density).

631

632

633

642

643

644

645

	Voronoi (DS1)	Voronoi (DS2)	Weighted average (DS1)	Weighted average (DS2)	Inversion on grain-size	Exponential fitting	Weibull fitting
Mdϕ	-1.9	-2.1	-1.9	-1.9	-1.8	-0.5	-0.7
$\sigma\phi$	2.4	2.7	2.0	2.0	2.1	3.5	3.8
wt% fine ash	8.7	12.9	6.9	7.1	ND	19.5	16.0
Mode of SP1	-2.2	-2.5	-2.1	-2.1	-1.9	-1.4	-1.5
Fraction of SP1	0.9	0.9	0.9	0.9	1.0	0.8	0.8
Mode of SP2	5.1	6.2	5.4	5.4	ND	ND	ND
Fraction of SP2	0.1	0.1	0.1	0.1	ND	ND	ND

646 **Table 1.** TGSD grain-size parameters as derived with different strategies and for different datasets (see

647 text for more details). Mdϕ and $\sigma\phi$ are from Inmann (1952). ND: not derivable. DS1 and DS2 are

648 dataset 1 and 2 in Appendix 3. SP1 and SP2 are coarse- and fine-grained sub-populations, respectively.

649

650

Appendix 1

Isomass maps of individual ϕ categories for Unit I (cumulative A to F layers) in kg m⁻²
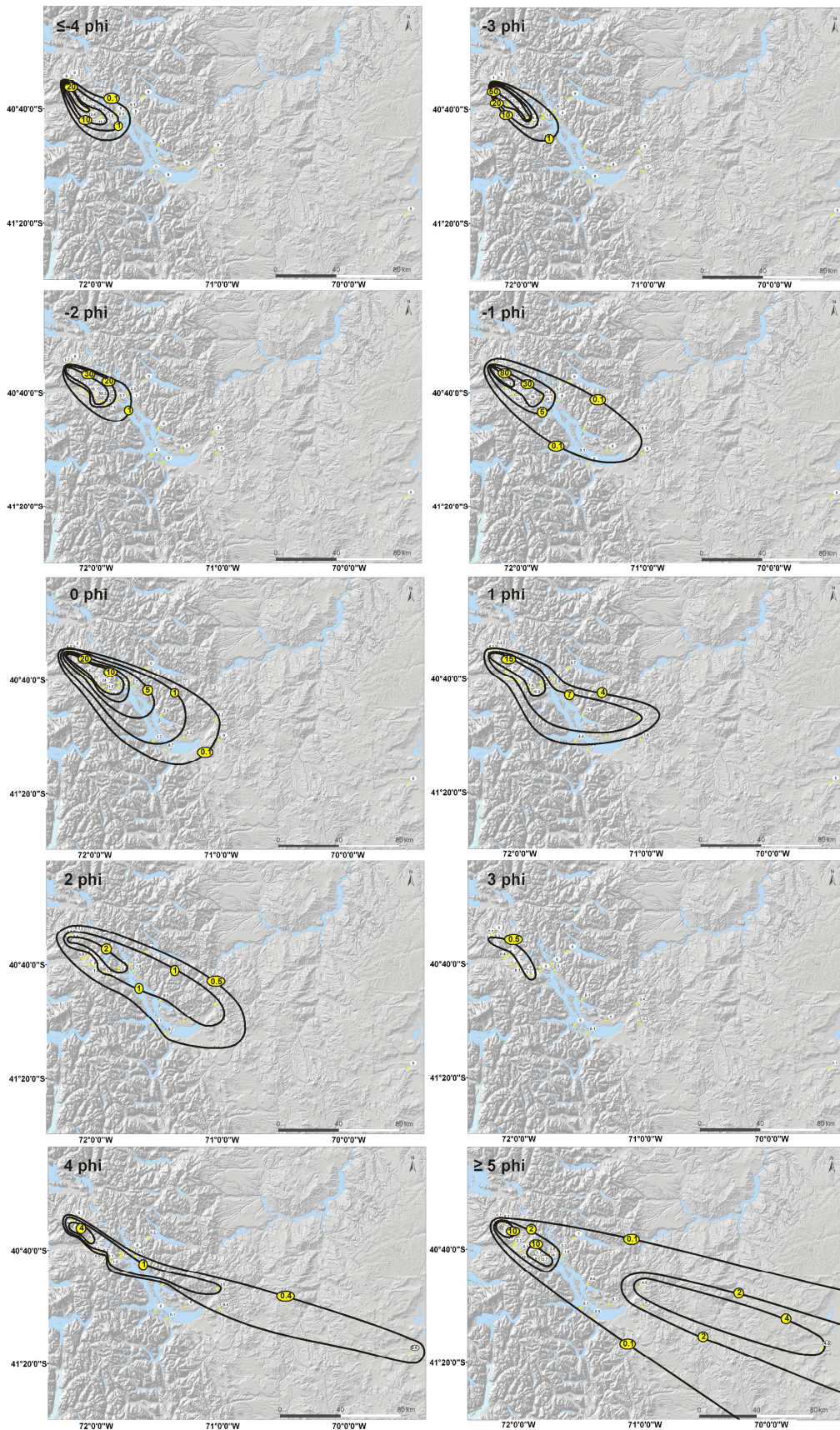
Appendix 2

Calculation of particle terminal velocity

657   Particle terminal velocity was calculated with the equation of Ganser (1993) for the mean diameter

658   within each half-ϕ size bin (assuming a Gaussian size distribution within each size bin) and averaged

659   over sedimentation height (1 to 14 km a.s.l. for A-F, 1 to 12 km a.s.l. for H and 1 to 10 km a.s.l. for

660   K2; maximum plume heights were considered for all phases). Sphericity was kept at 0.9 for both clast

661   categories (e.g. Folch 2012). Particle density was measured for individual clast sizes by Pistolesi et al.

662   (submitted) (see Figs 9b,e,h). In Fig. A2-1 we show results for individual layers A to F.
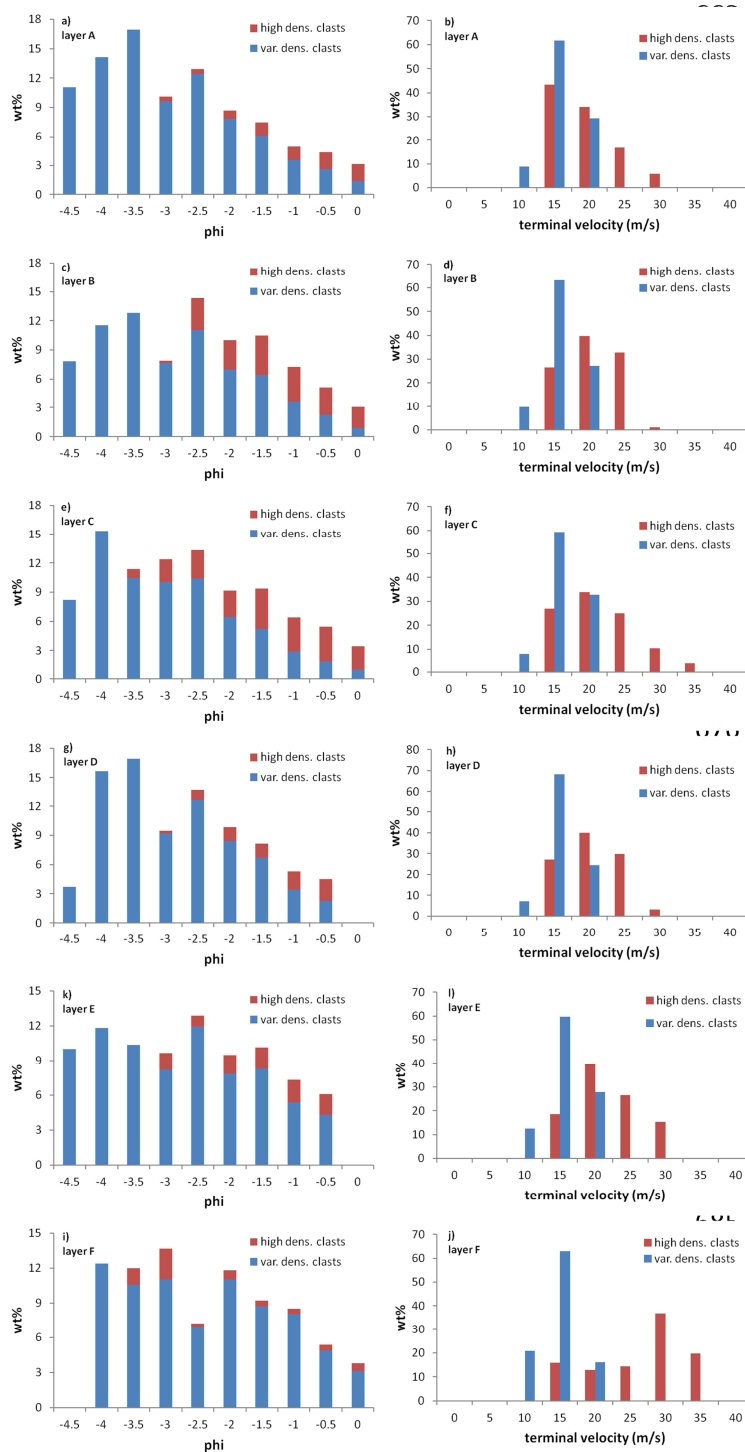
Fig. A2-1. Componentry (left column) and terminal velocity (right column) of tephra clasts ranging from 0 to -4.5 ϕ (i.e. 1-22.6 mm) for layers A to F at a locality about 15 km from vent on the dispersal axis for Unit I. See also Fig. 9 for results of the other layers.

Appendix 3

Calculation of the total grain-size distribution of Unit I

In order to account for the missing distal data in the derivation of the total grain-size distribution of the A-F cumulative layer (i.e. Unit I), we have derived the mass/area of 6 points about 600 km from vent from the isopach maps compiled soon after the eruption by Gáitan et al. (2011) and the INTA (2011). Based on these two maps that also describe the distal deposit, we assigned to the 6 distal data a thickness of 0.1 cm (i.e. 0.8 kg m^{-2} based on our most distal value of deposit density, i.e., 834 kg m^{-3}; Fig. 5) and the grain-size shown in Fig. A3-1. The two maps (based on dataset 1 and 2) are compared in Fig. A3-2.
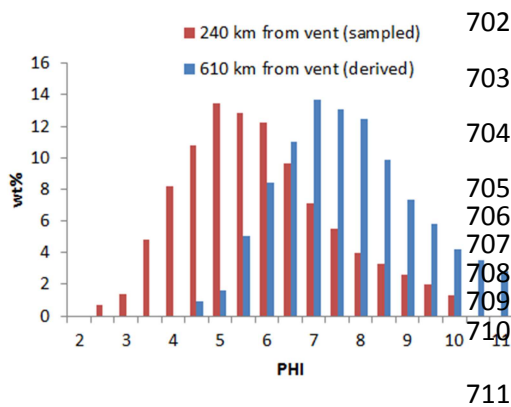
Fig. A3-1. Grain-size distribution derived for the distal points (610 km from vent; blue histograms) based on the distribution of our most distal sample at 240 km from vent (red histograms) and on the proportion of lapilli, coarse ash and fine ash as derived from the best-fit equations in Fig. 3a, main text (i.e. Gaussian distribution with mode of 7ϕ and composed of 99% fine ash).
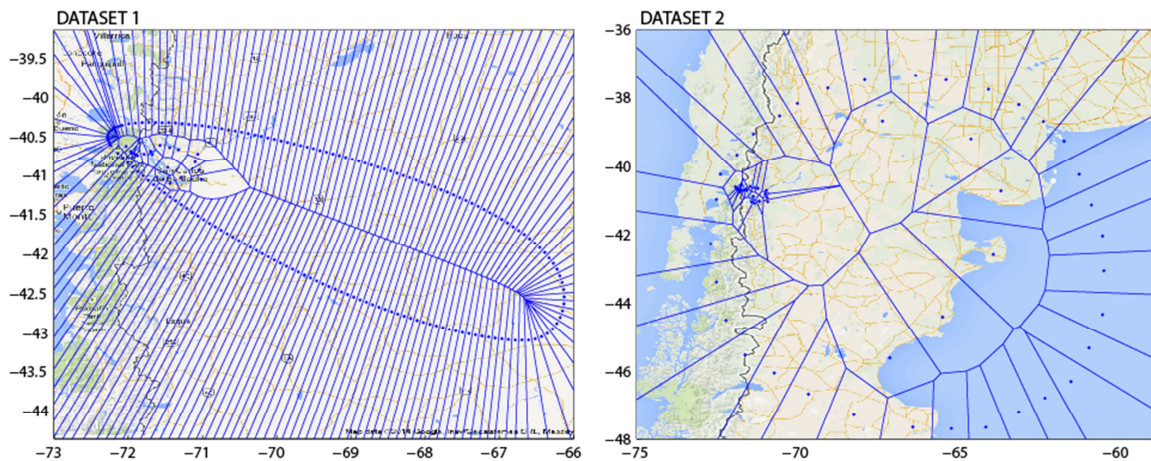

Fig. A3-2. Maps showing the Voronoi triangulation and the zero line used for the determination of the total grain-size distribution based on the Voronoi tessellation method of Bonadonna and Houghton (2005) and using the application of Biass and Bonadonna (2014) for: a) data-set 1 (i.e. samples collected in our field surveys) and b) data-set 2 (data-set 1 combined with six distal points derived from the isopach maps compiled soon after the eruption by Gáitan et al. (2011) and the INTA (2011)).

Appendix 4

719   **Inversion on grain-size using the model TEPHRA2**
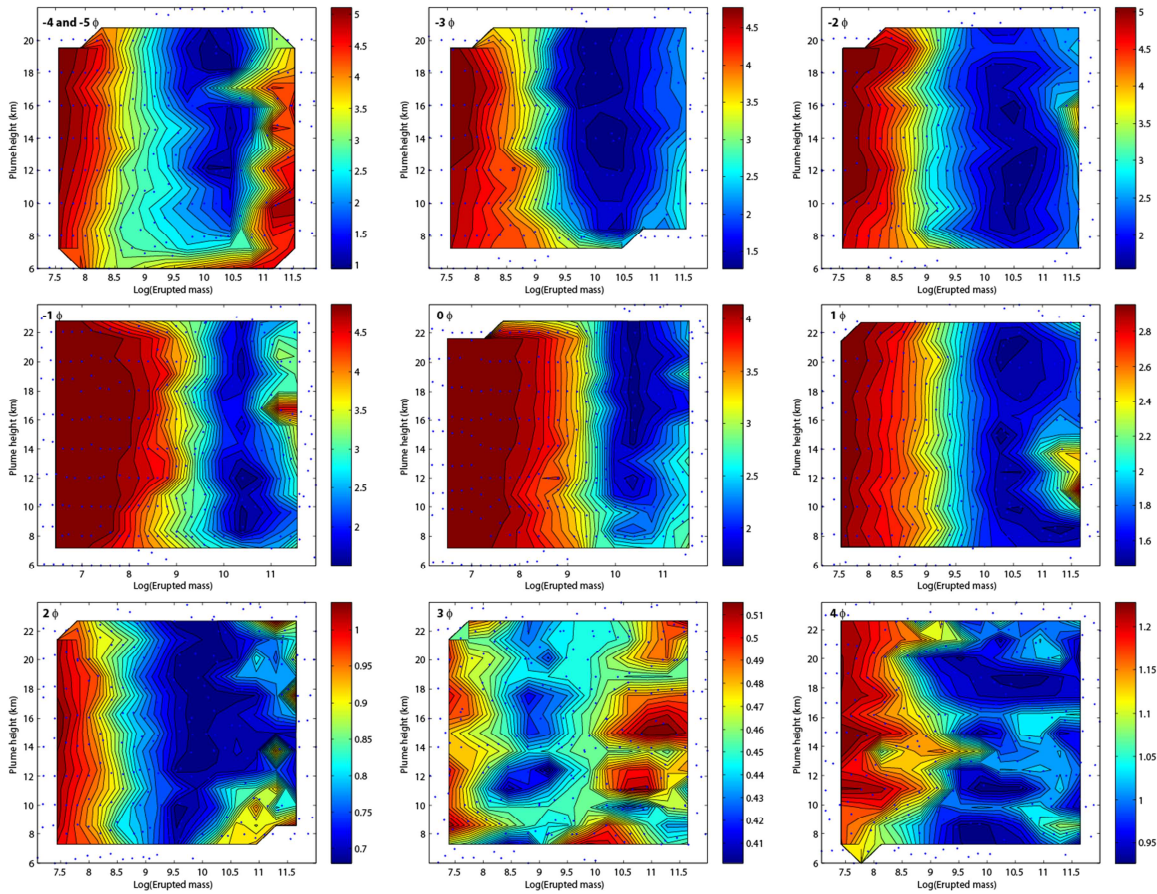
720

721   Fig. A4.1 Plot of Log(erupted mass) vs. plume height (km) (above sea level) showing the minimum values (dark blue) of the
722   goodness-of-fit measure (Root Mean Square Error, RMSE) associated with individual ϕ size categories (indicated in each plot)
723   of the climactic phase of Córdon Caulle eruption (i.e. Unit I).

724

725
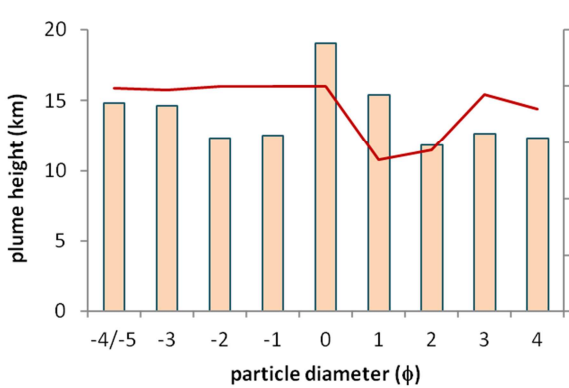
Fig. A4-2. Best-fit plume height above sea level as derived from inversion on individual grain-size categories (average value=13.9 km). The mass along the eruptive plume in the model TEPHRA2 is described by a beta function characterized by two parameters, α and β (Connor et al. 2015, in press). For simplicity, in these inversion calculations α is kept constant (i.e. 3) and β is left vary between 0.5 (i.e. particles are mostly released at the top of the cloud) and 2 (i.e. particles are released at a height which is 60-70% the total height). Average best-fit value for the climactic phase of Córdon Caulle eruption is 1.8 (i.e. particles are mostly released at a height which is 70% the total height).

740

741

References

Alfano F, Bonadonna C, Gurioli L (2012) Insights into eruption dynamics from textural analysis: the case of the May, 2008, Chaiten eruption. Bulletin of Volcanology 74(9):2095-2108

Alfano F, Bonadonna C, Connor CB, Volentik A (submitted) From tephra grain-size and dispersal to magma fragmentation: the case of the 2008 Chaitén rhyolitic eruption, Chile. Bulletin of Volcanology

Bonadonna C, Mayberry GC, Calder ES, et al. (2002) Tephra fallout in the eruption of Soufrière Hills Volcano, Montserrat. In: Druitt TH, Kokelaar BP (eds) The eruption of Soufrière Hills Volcano, Montserrat, from 1995 to 1999. Geological Society, London, Memoir, pp 483-516

Bonadonna C, Houghton BF (2005) Total grainsize distribution and volume of tephra-fall deposits. Bulletin of Volcanology 67:441-456

Bonadonna C, Phillips JC, Houghton BF (2005) Modeling tephra sedimentation from a Ruapehu weak plume eruption. Journal of Geophysical Research 110(B8, B08209)

Bonadonna C, Genco R, Gouhier M, et al. (2011) Tephra sedimentation during the 2010 Eyjafjallajokull eruption (Iceland) from deposit, radar, and satellite observations. Journal of Geophysical Research-Solid Earth 116

Bonadonna C, Costa A (2012) Estimating the volume of tephra deposits: A new simple strategy. Geology 40(5):415-418

Bonadonna C, Cioni R, Pistolesi M, et al. (2013) Determination of the largest clast sizes of tephra deposits for the characterization of explosive eruptions: a study of the IAVCEI commission on tephra hazard modelling. Bulletin of Volcanology 75(1)

Bonadonna C, Pistolesi M, Cioni R, et al. (2015, in press) Dynamics of wind-affected volcanic plumes: the example of the 2011 Cordón Caulle eruption, Chile. Journal of Geophysical Research

Brazier S, Sparks RSJ, Carey SN, et al. (1983) Bimodal grain-size distribution and secondary thickening in air-fall ash layers. Nature 301(5896):115-119

Brown RJ, Bonadonna C, Durant AJ (2012) A Review of Volcanic Ash Aggregation. Physics and Chemistry of the Earth 45-46:65-78

Carazzo G, Jellinek AM (2012) A new view of the dynamics, stability and longevity of volcanic clouds. Earth and Planetary Science Letters 325:39-51

Carazzo G, Jellinek AM (2013) Particle sedimentation and diffusive convection in volcanic ash-clouds. Journal of Geophysical Research-Solid Earth 118(4):1420-1437

774   Carey SN, Sigurdsson H (1982) Influence of particle aggregation on deposition of distal tephra from

775   the May 18, 1980, eruption of Mount St-Helens volcano. Journal of Geophysical Research

776   87(B8):7061-7072

777   Castro JM, Schipper CI, Mueller SP, et al. (2013) Storage and eruption of near-liquidus rhyolite

778   magma at Cordon Caulle, Chile. Bulletin of Volcanology 75(4)

779   Collini E, Osores SM, Folch A, et al. (2013) Volcanic ash forecast during the June 2011 Cordon Caulle

780   eruption. Natural Hazards 66(2):389-412

781   Connor CB, Connor LJ, Bonadonna C, Luhr JF, Savov IP, Navarro-Ochoa C (2015, in press) Modeling

782   Tephra Thickness and Particle Size Distribution of the 1913 Eruption of Volcan de Colima, Mexico.

783   In: Varley N, Komorowski JC (eds) Volcan de Colima - Managing the threat. Springer Verlag for the

784   IAVCEI in the Active Volcanoes of the World Series

785   Dingwell DB, Lavallee Y, Kueppers U (2012) Volcanic ash: A primary agent in the Earth system.

786   Physics and Chemistry of the Earth 45-46:2-4

787   Dufek J, Manga M, Patel A (2012) Granular disruption during explosive volcanic eruptions. Nature

788   Geoscience 5(8):561-564

789   Durant AJ, Rose WI (2009) Sedimentological constraints on hydrometeor-enhanced particle

790   deposition: 1992 Eruptions of Crater Peak, Alaska. Journal of Volcanology and Geothermal

791   Research 186(1-2):40-59

792   Durant AJ, Rose WI, Sarna-Wojcicki AM, et al. (2009) Hydrometeor-enhanced tephra sedimentation:

793   Constraints from the 18 May 1980 eruption of Mount St. Helens. Journal of Geophysical Research-

794   Solid Earth 114

795   Durant AJ, Villarosa G, Rose WI, et al. (2012) Long-range volcanic ash transport and fallout during the

796   2008 eruption of Chaiten volcano, Chile. Physics and Chemistry of the Earth 45-46:50-64

797   Eychenne J, Le Pennec J-L, Troncoso L, et al. (2012) Causes and consequences of bimodal grain-size

798   distribution of tephra fall deposited during the August 2006 Tungurahua eruption (Ecuador).

799   Bulletin of Volcanology 74(1):187-205

800   Fisher RV, Schmincke HU (1984) Pyroclastic rocks. pp xiv+472 pp-xiv+472 pp

801   Folch A (2012) A review of tephra transport and dispersal models: Evolution, current status, and

802   future perspectives. Journal of Volcanology and Geothermal Research 235:96-115

803   Folch A, Mingari L, Osores MS, Collini E (2014) Modeling volcanic ash resuspension - application to

804   the 14-18 October 2011 outbreak episode in central Patagonia, Argentina. Natural Hazards and

805   Earth System Sciences 14(1):119-133

806   Fontijn K, Ernst GGJ, Bonadonna C, et al. (2011) The 4-ka Rungwe Pumice (South-Western Tanzania):

807   a wind-still Plinian eruption. Bulletin of Volcanology 73(9):1353-1368

808   Gaitán JJ, Ayesa JA, Umaña F, Raffo F, Bran DB (2011) Cartografía del área afectada por cenizas

809   volcánicas en las provincias de Río Negro y Neuquén. In: INTA

810   http://inta.gob.ar/documentos/cartografia-del-area-afectada-por-cenizas-volcanicas-en-las-

811   provincias-de-rio-negro-y-neuquen/,

812   Ganser GH (1993) A rational approach to drag prediction of spherical and nonspherical particles.

813   Powder Technology 77(2):143-152

814   Hadley D, Hufford GL, Simpson JJ (2004) Resuspension of relic volcanic ash and dust from Katmai:

815   Still an aviation hazard. Weather and Forecasting 19(5):829-840

816   Hildreth W, Drake RE (1992) Volcano Quizapu, Chilean Andes. Bulletin of Volcanology 54:93-125

817   Hincks TK, Aspinall WP, Baxter PJ, et al. (2006) Long term exposure to respirable volcanic ash on

818   Montserrat: a time series simulation. Bulletin of Volcanology 68(3):266-284

819   Hobbs PV, Hegg DA, Radke LF (1983) Resuspension of volcanic ash from Mount St-Helens. Journal of

820   Geophysical Research-Oceans and Atmospheres 88(NC6):3919-3921

821   Inman DL (1952) Measures for describing the size distribution of sediments. Journal of Sedimentary

822   Petrology 22:125-145

823   Kaminski E, Jaupart C (1998) The size distribution of pyroclasts and the fragmentation sequence in

824   explosive volcanic eruptions. Journal of Geophysical Research-Solid Earth 103(B12):29759-29779

825   Kueppers U, Scheu B, Spieler O, Dingwell DB (2006) Fragmentation efficiency of explosive volcanic

826   eruptions: A study of experimentally generated pyroclasts. Journal of Volcanology and Geothermal

827   Research 153(1-2):125-135

828   Leadbetter SJ, Hort MC, von Lowis S, et al. (2012) Modeling the resuspension of ash deposited during

829   the eruption of Eyjafjallajokull in spring 2010. Journal of Geophysical Research-Atmospheres 117

830   Legros F (2000) Minimum volume of a tephra fallout deposit estimated from a single isopach. Journal

831   of Volcanology and Geothermal Resarch 96:25-32

832   Manzella I, Bonadonna C, Phillips JC, Monnard H (2015, in press) The role of gravitational instabilities

833   in depositing volcanic ash. Geology

834   Murrow PJ, Rose WI, Self S (1980) Determination of the Total Grain-Size Distribution in a Vulcanian

835   Eruption Column, and Its Implications to Stratospheric Aerosol Perturbation. Geophysical Research

836   Letters 7(11):893-896

837   Perugini D, Speziali A, Caricchi L, Kueppers U (2011) Application of fractal fragmentation theory to

838   natural pyroclastic deposits: Insights into volcanic explosivity of the Valentano scoria cone (Italy).

839   Journal of Volcanology and Geothermal Research 202(3-4):200-210

840   Pistolesi M, Cioni R, Bonadonna C, et al. (submitted) Complex dynamics of small-moderate volcanic

841   events: the example of the 2011 rhyolitic Cordón Caulle eruption, Chile. Bulletin of Volcanology

842   Prata AJ, Grant IF (2001) Retrieval of microphysical and morphological properties of volcanic ash

843   plumes from satellite data: Application to Mt Ruapehu, New Zealand. Quarterly Journal of the

844   Royal Meteorological Society 127(576):2153-2179

845   Pyle DM (1989) The thickness, volume and grainsize of tephra fall deposits. Bulletin of Volcanology

846   51(1):1-15

847   Rose WI, Self S, Murrow PJ, et al. (2007) Nature and significance of small volume fall deposits at

848   composite volcanoes: Insights from the October 14, 1974 Fuego eruption, Guatemala. Bulletin of

849   Volcanology

850   Rust AC, Cashman KV (2011) Permeability controls on expansion and size distributions of pyroclasts.

851   Journal of Geophysical Research-Solid Earth 116

852   Scasso R, Corbella H, Tiberi P (1994) Sedimentological analysis of the tephra from 12-15 August 1991

853   eruption of Hudson Volcano. Bulletin of Volcanology 56:121-132

854   Schipper CI, Castro JM, Tuffen H, James MR, How P (2013) Shallow vent architecture during hybrid

855   explosive-effusive activity at Cordón Caulle (Chile, 2011-12): Evidence from direct observations and

856   pyroclast textures. J Volc Geoth Res 262:25-37. doi:10.1016/j.jvolgeores.2013.06.005

857   Scollo S, Del Carlo P, Coltelli M (2007) Tephra fallout of 2001 Etna flank eruption: Analysis of the

858   deposit and plume dispersion. Journal of Volcanology and Geothermal Research 160(1-2):147-164

859   SERNAGEOMIN/OVDAS (2011) Puyehue - Cordón Caulle: Reporte especial de actividad volcánica

860   No31. In: http://www.sernageomin.cl/volcan.php?pagina=7&iId=38,

861   Sparks RSJ, Wilson L, Sigurdsson H (1981) The pyroclastic deposits of the 1875 eruption of Askja,

862   Iceland. Philosophical Transaction of the Royal Society of London 229:241-273

863   Thorsteinsson T, Johannsson T, Stohl A, Kristiansen NI (2012) High levels of particulate matter in

864   Iceland due to direct ash emissions by the Eyjafjallajokull eruption and resuspension of deposited

865   ash. Journal of Geophysical Research-Solid Earth 117

866   Varekamp JC, Luhr JF, Prestegaard KL (1984) The 1982 Eruptions of El-Chichon Volcano (Chiapas,

867   Mexico) - Character of the Eruptions, Ash-Fall Deposits, and Gas-Phase. Journal of Volcanology and

868   Geothermal Research 23(1-2):39-68

869   Volentik ACM, Bonadonna C, Connor CB, et al. (2010) Modeling tephra dispersal in absence of wind:

870   Insights from the climactic phase of the 2450 BP Plinian eruption of Pululagua volcano (Ecuador).

871   Journal of Volcanology and Geothermal Research 193(1-2):117-136

872   Waitt RB, Jr., Hansen VL, Sarna-Wojcicki AM, Wood SH (1981) Proximal air-fall deposits of eruptions

873   between May 24 and August 7, 1980-stratigraphy and field sedimentology Mount St. Helens. In:

874   Lipman PW, Mullineaux DR (eds) The 1980 eruptions of Mount St. Helens, Washington. U.S.

875   Geological Survey Professional Paper Washington, D.C., pp 617-628

876   Walker GPL (1981) Characteristics of two phreatoplinian ashes, and their water-flushed origin.

877   Journal of Volcanology and Geothermal Research 9:395-407

878   Wiesner MG, Wetzel A, Catane SG, et al. (2004) Grain size, areal thickness distribution and controls

879   on sedimentation of the 1991 Mount Pinatubo tephra layer in the South China Sea. Bulletin of

880   Volcanology 66(3):226-242

881   Wilson TM, Cole JW, Stewart C, et al. (2011) Ash storms: impacts of wind-remobilised volcanic ash

882   on rural communities and agriculture following the 1991 Hudson eruption, southern Patagonia,

883   Chile. Bulletin of Volcanology 73(3):223-239

884   Wilson TM, Stewart C, Bickerton H, et al. (2013) Impacts of the June 2011 Puyehue-Cordon Caulle

885   volcanic complex eruption on urban infrastucture, agricolture and public health. In: GNS Science

886   Report 2012/20.

887   Wohletz KH, Sheridan MF, Brown WK (1989) Particle-size distributions and the sequential

888   fragmentation/transport theory applied to volcanic ash. Journal of Geophysical Research-Solid

889   Earth and Planets 94(B11):15703-15721

890

891